AIAA JOURNAL
Vol. 34, No. 5, May 1996

Computation of Sound Radiating from Engine Inlets

Yusuf Özyörük* and Lyle N. Long†
Pennsylvania State University, University Park, Pennsylvania 16802-1401

A hybrid method has been developed to calculate sound radiation from turbofan engine inlets. Given the acoustic source at an interface near the fan, the method solves the full three-dimensional, time-dependent Euler equations in the near field and passes the solution to a moving-surface Kirchhoff method for far-field predictions. The Kirchhoff method enables one to limit the size of the computational domain where the essential acoustic signals are captured accurately by a high-order accurate flow solver and then to extrapolate these signals to the far field exactly only within the discretization error on the Kirchhoff surface. The steady flowfield is required by the hybrid approach and a high-order accurate multigrid method has been implemented to enhance convergence of steady-state calculations. The computations are all carried out on parallel processors using essentially high-performance Fortran language. Results indicate very good agreement with available numerical and analytical solutions.

Nomenclature

$A_{nm\mu}$	= Fourier coefficients
B	= number of rotor blades
c	= speed of sound
$\boldsymbol{E}, \boldsymbol{F}, \boldsymbol{G}$	= functions of $\boldsymbol{Q}$
f	= frequency
i	= $\sqrt{(-1)}$
J	= Jacobian
J_m	= Bessel function of order m
k	= wave number
$k_{m\mu}$	= radial wave number
$M, \boldsymbol{M}$	= Mach number, Mach number vector
M_T	= rotor tip Mach number
m	= circumferential mode order
NE	= number of Kirchhoff surface elements
n	= time step level; or time harmonic index
$\hat{n}$	= normal vector
P	= discretized integrand; Eq. (12)
$p, \bar{p}$	= pressure, mean pressure
$\boldsymbol{Q}$	= vector of dependent variables
$\boldsymbol{R}$	= source-observer distance vector
$\boldsymbol{S}_B, \boldsymbol{S}_C$	= source vectors, functions of $\boldsymbol{Q}$
t	= time
(u_1, u_2, u_3)	= velocity components
V	= number of stator vanes
$\boldsymbol{V}$	= velocity
x	= axial distance
(x_1, x_2, x_3)	= Cartesian or cylindrical coordinates, (x, y, z) or (x, r, θ)
$\boldsymbol{x}$	= observer position vector
$\boldsymbol{y}$	= surface element position vector
ΔS	= Kirchhoff surface element area
Δt	= time increment
θ	= polar angle, or angle from inlet axis
ϑ	= angle between $\hat{n}$ and $\boldsymbol{R}$
μ	= radial mode order
ν	= coordinate system switch, 0 for Cartesian coordinates and 1 for cylindrical coordinates
(ξ, η, ζ)	= curvilinear coordinates
$\xi_{m\mu}$	= cutoff ratio
ρ	= density
ρe	= total energy
τ	= retarded time, source time
$\phi_{nm\mu}$	= phase angle
ω	= circular frequency

Subscripts

e	= Kirchhoff surface element
f	= fan stage
∞	= freestream

Superscripts

$n*$	= emission time step level
$'$	= acoustic quantity
$*$	= emission time

Received July 14, 1995; revision received Dec. 27, 1995; accepted for publication Jan. 8, 1996.

*Graduate Research Assistant, Department of Aerospace Engineering; currently Postdoctoral Scholar, Department of Aerospace Engineering. Member AIAA.

†Associate Professor, Department of Aerospace Engineering. Senior Member AIAA.

I. Introduction

FAN noise has a pronounced role in the overall noise signature of ultrahigh bypass ratio turbofan engines. These engines will power future, large, advanced subsonic transport aircraft. Reduction of fan noise is necessary to meet the stringent community noise regulations. There exists ongoing research activity to develop fan noise prediction systems.[1–7]

At high power settings of a turbofan engine, the flow Mach number in the inlet can be significantly high. In addition, the acoustic perturbations can be large. Consequently, nonlinear and aerodynamic-acoustic coupling effects on the acoustic propagation and radiation process can be important. However, most of the fan noise analysis systems are based on the linearized methods.

One important method utilizes the combination of the finite element (FE) and wave envelope (WE) techniques with two-dimensional (axisymmetric) velocity potential formulations.[1,2] The aerodynamic and acoustic field equations are decoupled in this method. Therefore, the FE–WE method does not account for aerodynamic-acoustic coupling and nonlinear effects. Also, because of its two-dimensional formulations in the frequency domain, calculations with multiple circumferential modes are performed separately for each individual mode.[4] Nonetheless this method is one of the most widely used methods in fan noise prediction systems.[4,5]

Boundary element methods (BEM) have recently gained popularity for their speed and effectiveness in the computation of ducted fan noise.[6,8] However, the flow and acoustic field equations are decoupled in these methods as well, and the background flow is assumed uniform. Another fast technique is based on ray tracing,[7] which works well at high frequencies.

The current research concentrates on the development of a hybrid, high-order accurate, time-domain method that can address all of the aforementioned important issues. The nonuniform background flow and aerodynamic-acoustic coupling effects are all accounted for by

solving the full nonlinear Euler equations in the time domain on a curvilinear coordinate system with which fully three-dimensional engine nacelles can be treated. The method can accept, as the source, superposition of multiple modes and harmonics of the blade passing frequency. Computations are carried out on parallel processors that offer high computational power.

As the solution of the Euler equations is obtained, it is passed to a Kirchhoff method to obtain the far-field noise. This method is based on the moving surface Kirchhoff's formula of Farassat and Myers.[9] It essentially needs the past-time histories of the acoustic pressure and its temporal and spatial derivatives on a closed surface. Previous numerical implementations[10,11] performed the Kirchhoff surface integrations at the retarded times. In this paper, a recursive summation of the acoustic pressure contributions from Kirchhoff surface elements is performed as soon as the Euler solution becomes available. This procedure prevents having to save large spectra of past-time data on the Kirchhoff surface.

In the following, the Euler solver is briefly described, and the acoustic source model is discussed. Then the Kirchhoff method and its coupling with the flow solver are described. Finally, results for some realistic problems are presented and compared with available numerical and exact solutions. It is shown that the hybrid method is capable of accurately solving problems with various kr as high as 25.

II. Algorithms

A. Flowfield Solver and Fan-Face Conditions

The three-dimensional Euler equations are solved in the interior of the computational domain, and nonreflecting boundary conditions are solved on the far-field boundaries using a temporally and spatially fourth-order accurate, finite difference, Runge–Kutta (R–K) time integration scheme. The nonreflecting boundary conditions used are based on the B_1 operator of Bayliss and Turkel[12] on the inflow boundaries and the B_1 operator and the linearized Euler equations on the outflow boundaries, similarly to Tam and Webb.[13] To use the same integration scheme across the entire domain, the interior and the far-field boundary equations are all written in the same differential form, with a choice of the Cartesian or cylindrical coordinate system:

$$\frac{\partial \boldsymbol{Q}}{\partial t}+\frac{\partial \boldsymbol{E}}{\partial x_1}+\frac{\partial \boldsymbol{F}}{\partial x_2}+\frac{1}{x_2^{\nu}}\frac{\partial \boldsymbol{G}}{\partial x_3}+\frac{\boldsymbol{S}_B+\nu \boldsymbol{S}_C}{x_2^{\nu}}=0 \tag{1}$$

The vector of state variables for the interior points is $\boldsymbol{Q}_{\text{int}} = [\rho, \rho u_1, \rho u_2, \rho u_3, \rho e]^T$ and for the radiation and outflow boundary points $\boldsymbol{Q}_{\text{rad,out}} = [\rho', u_1', u_2', u_3', p']^T$, where a prime indicates the deviation from the undisturbed (freestream) value of the associated quantity. The pressure is given by the equation of state as $p = (\gamma-1)[\rho e - \frac{1}{2}\rho(u_1^2+u_2^2+u_3^2)]$. The terms $\boldsymbol{E}, \boldsymbol{F}, \boldsymbol{G}$, and $\boldsymbol{S}$ for the Euler equations can be found in many standard fluid dynamics text books, and these terms for the far-field boundary conditions are given in the Appendix of Ref. 14.

The physical domain is mapped onto a uniform computational domain using a three-dimensional, body-fitted, curvilinear coordinate system:

$$x_1 = x_1(\xi,\eta,\zeta), \qquad x_2 = x_2(\xi,\eta,\zeta), \qquad x_3 = x_3(\xi,\eta,\zeta) \tag{2}$$

With this transformation, the governing equations [Eq. (1)] take the following form:

$$\frac{\partial}{\partial t}\frac{\boldsymbol{Q}}{J}+\frac{\partial \tilde{\boldsymbol{E}}}{\partial \xi}+\frac{\partial \tilde{\boldsymbol{F}}}{\partial \eta}+\frac{\partial \tilde{\boldsymbol{G}}}{\partial \zeta}+\frac{\boldsymbol{S}_B+\nu \boldsymbol{S}_C}{J x_2^{\nu}}=0 \tag{3}$$

where

$$\begin{Bmatrix}\tilde{\boldsymbol{E}}\\ \tilde{\boldsymbol{F}}\\ \tilde{\boldsymbol{G}}\end{Bmatrix}=\frac{1}{J}\begin{bmatrix}\xi_{x_1} & \xi_{x_2} & x_2^{-\nu}\xi_{x_3}\\ \eta_{x_1} & \eta_{x_2} & x_2^{-\nu}\eta_{x_3}\\ \zeta_{x_1} & \zeta_{x_2} & x_2^{-\nu}\zeta_{x_3}\end{bmatrix}\begin{Bmatrix}\boldsymbol{E}\\ \boldsymbol{F}\\ \boldsymbol{G}\end{Bmatrix} \tag{4}$$

The Jacobian of the coordinate transformation is given by

$$J^{-1} = |\partial(x_1,x_2,x_3)/\partial(\xi,\eta,\zeta)| \tag{5}$$

The metric quantities are

$$\begin{bmatrix}\xi_{x_1} & \xi_{x_2} & \xi_{x_3}\\ \eta_{x_1} & \eta_{x_2} & \eta_{x_3}\\ \zeta_{x_1} & \zeta_{x_2} & \zeta_{x_3}\end{bmatrix}=\begin{bmatrix}x_{1_\xi} & x_{1_\eta} & x_{1_\zeta}\\ x_{2_\xi} & x_{2_\eta} & x_{2_\zeta}\\ x_{3_\xi} & x_{3_\eta} & x_{3_\zeta}\end{bmatrix}^{-1} \tag{6}$$

The spatial derivatives of Eq. (3) are computed using fourth-order accurate finite differences, as central in the interior, and biased at or near the boundaries. These derivatives are evaluated simultaneously at the interior and far-field boundary points, taking advantage of the parallel processing capability. To avoid zero Jacobians in the equations, the grid system is constructed such that no grid points exist at the singular positions. Equation (3) is then integrated in time using the classical, four-stage R–K technique, with addition of artificial dissipation to the residuals of the governing equations to suppress spurious oscillations. The acoustic pressure field is obtained by the subtraction of the mean field. The required steady-state computations are carried out using a spatially fourth-order accurate multigrid method. More detail on the current algorithm for the flow solver can be found in Refs. 14 and 15.

Only one characteristic enters the inlet domain from the fan-face (source plane). This characteristic is associated with the acoustic waves that are induced mostly by the fan blade loadings and rotor-stator interactions.[16] Therefore, the specification of either the pressure or mass flux is sufficient for the boundary condition closure. The other dependent variables are solved from the interior equations. Most often the time-dependent fan-face pressure is modeled[3,4,17] and used as the input to the available inlet radiation codes.[1] Direct aerodynamic computations are sometimes performed[5] to determine the source as well. In this paper we model the source using the standard eigensolutions of the convective wave equation for infinitely long cylindrical ducts. However, because of the current method's time-domain approach, there is no restriction to the specification of any arbitrary external source.

The source plane acoustic pressure as represented by the superposition of the circular duct eigensolutions is given by

$$p_f'(x,r,\theta,t) = \Re\left(\sum_{n=1}^{\infty}\sum_{m=-\infty}^{\infty}\sum_{\mu=0}^{\infty}\hat{p}_{nm\mu}e^{-i\omega nt}\right) \tag{7}$$

where

$$\hat{p}_{nm\mu} = A_{nm\mu}\,J_m(k_{m\mu}r)\exp[i(k_{x,m\mu}x + m\theta + \phi_{nm\mu})] \tag{8}$$

with the axial wave number

$$k_{x,m\mu} = \frac{-M_f k - \sqrt{k^2-(1-M_f^2)k_{m\mu}^2}}{1-M_f^2} \tag{9}$$

In the preceding source model, only the upstream-propagating (negative x direction) wave components are considered, and the downstream-propagating components are ignored. However, should there be any downstream propagating modes because of the various impedance mismatches because of the changing local conditions in the duct, these modes should pass the fan-face boundary without any reflections. This is true when the Euler equations are discretized properly at the boundary. Only here is it assumed that the downstream propagating waves do not interact with the fan and therefore do not produce noise.

An individual wave is usually characterized by its circumferential and radial mode orders as the (m, μ) mode. It is clear from Eqs. (8) and (9) that whether the (m, μ) mode will propagate (cut on) or exponentially decay (cut off) is determined by its axial wave number $k_{x,m\mu}$, more specifically by the terms of the radical in Eq. (9). A single parameter is usually defined for this. It is called the cutoff ratio and given by

$$\xi_{m\mu} = \frac{nBM_T}{r_f k_{m\mu}\sqrt{1-M_f^2}} \tag{10}$$

Thus, the (m, μ) mode is cut on if $\xi_{m\mu} \geq 1$.

A detailed theory of the modes that are generated in and radiated from an engine inlet is given by Tyler and Sofrin.[16] Their analysis of rotor-stator interactions indicates that the circumferential order m is related to the number of rotor blades and the number of stator vanes by the equation

$$m = nB + sV, \qquad s = \ldots, -1, 0, 1, \ldots \tag{11}$$

Thus the summation over the circumferential mode m in Eq. (7) is usually performed only for those modes given by Eq. (11).

The pressure at the fan is then given by $p_f = \bar{p}_f + p'_f$, where the mean pressure $\bar{p}_f$ is obtained using the one-dimensional ideal gasdynamics relations given the engine operating conditions (mass flow rate, freestream Mach number, etc.) described in Özyörük.[15]

B. Coupling with Kirchhoff Method

In the far-field prediction of an aeroacoustics problem, it is almost always essential to use a far-field extrapolation technique. This is because a direct simulation requires an extremely large computational domain that in turn implies enormous computational resources and perhaps most importantly very large numerical error because of dissipation and dispersion. Therefore, Kirchhoff methods have recently found increasing use in flow-induced far-field noise predictions.[18,19] In the current method, the near-field Euler solution given on a closed Kirchhoff surface is extrapolated to the far-field observer point assuming that the field between the two regions is governed by the linear wave equation.

A review of the Kirchhoff methods used in the literature is given by Lyrintzis.[20] Here the Kirchhoff formula developed by Farassat and Myers[9] for arbitrarily moving and deforming surfaces is used and coupled with the Euler solver of the current method. For a nondeforming Kirchhoff surface that is in rectilinear motion, the Kirchhoff formula for the acoustic pressure p' at the observer location $\boldsymbol{x}$ and observer time t takes the following form:

$$4\pi p'(\boldsymbol{x}, t) = \int\int_S \left[\frac{E_1}{R(1-M_R)} + \frac{p' E_2}{R^2(1-M_R)}\right]_{\tau^*} \mathrm{d}S \tag{12}$$

where $R = |\boldsymbol{R}|$, $\boldsymbol{R} = \boldsymbol{x} - \boldsymbol{y}(\tau)$, $M_R = \boldsymbol{M} \cdot \boldsymbol{R}/R$, and

$$E_1 = -\hat{n} \cdot \nabla p' + (\boldsymbol{M} \cdot \hat{n})\,(\boldsymbol{M} \cdot \nabla p') + \left[\frac{\cos\vartheta - \boldsymbol{M} \cdot \hat{n}}{c_\infty(1-M_R)} - \frac{\boldsymbol{M} \cdot \hat{n}}{c_\infty}\right]\frac{\partial p'}{\partial \tau} \tag{13}$$

$$E_2 = \frac{1 - M^2}{(1-M_R)^2}(\cos\vartheta - \boldsymbol{M} \cdot \hat{n}) \tag{14}$$

The E_2 term was originally given in a somewhat complicated form in Farassat and Myers[9] but later was found by Myers and Hausmann[21] to reduce to the form of Eq. (14). The integrand of Eq. (12) is to be evaluated at the Kirchhoff surface point emission time τ^*, which is given by the root of

$$\tau - t + R(\tau)/c_\infty = 0 \tag{15}$$

The Kirchhoff surface is constructed out of the computational fluid dynamics (CFD) grid by specifying constant ξ, η, and/or ζ surfaces. For example, Fig. 1 shows a constant-ξ surface of the CFD grid, which can be used as the Kirchhoff surface. Equation (12) requires the surface parameters, such as the normal vector and surface element area. This information is directly related to the metrics given by Eq. (6). The computational mesh for the flow solver is generated using a sequence of conformal transformations, and the resulting grid system is orthogonal everywhere.[15] Thus, the normal vector on the Kirchhoff surface or a constant-ξ surface is given by $\hat{n} = \nabla\xi/|\nabla\xi|$, and a surface element area is given by $\Delta S = x_2^v J^{-1}|\nabla\xi|$.

In most problems the observer and the Kirchhoff surface are fixed relative to each other. Also the coordinate system is attached to the moving surface rather than the fluid. In this case the fluid passes both the observer and the Kirchhoff surface at the same speed, M_∞. Thus, the Kirchhoff surface and the observer are seen to travel at $-M_\infty$, and the elapsed time for a signal to travel from a

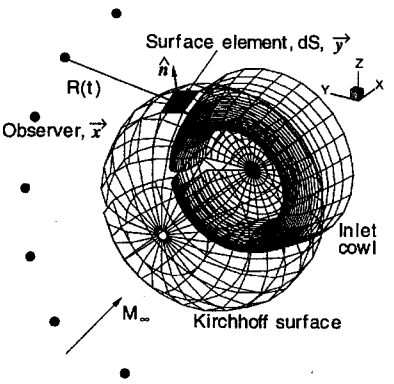

Fig. 1 Configuration for the hybrid inlet radiation method with multiple far-field observers. The Kirchhoff surface terminates at the cowl wall near the leading edge.

Kirchhoff surface element to the observer will always be the same. This greatly simplifies the numerical coupling of the flow solver and the Kirchhoff method. Thus, the emission time for a Kirchhoff surface element e is given by

$$\tau_e^* = t - R_e/c_\infty \tag{16}$$

where

$$R_e = \frac{-(\bar{x}_1 - \bar{y}_1)M_\infty + \bar{R}}{\beta^2} \tag{17}$$

with $\beta^2 = 1 - M_\infty^2$ and

$$\bar{R} = \sqrt{(\bar{x}_1 - \bar{y}_1)^2 + \beta^2\left[(\bar{x}_2 - \bar{y}_2)^2 + (\bar{x}_3 - \bar{y}_3)^2\right]} \tag{18}$$

in which $\bar{x}_1$ and $\bar{y}_1$ are the projected components of the vectors $\boldsymbol{x}$ and $\boldsymbol{y}$ on the Mach number vector $\boldsymbol{M}$, respectively, at the observer time. The components $\bar{x}_2$, $\bar{x}_3$ and $\bar{y}_2$, $\bar{y}_3$ are the transverse components to $\bar{x}_1$ and $\bar{y}_1$, respectively.

The Kirchhoff surface integrations are performed assuming that the integrand in Eq. (12) is constant over a Kirchhoff surface element, and the time is discretized in the same manner as in the flow solver. The acoustic pressure required by Eq. (12) in the vicinity of the Kirchhoff surface is obtained from the flow solver by subtracting the mean pressure from the instantaneous pressure. In most cases the time increment of the flow solver, Δt, from one time step to the next is sufficiently small to calculate the time derivative of the acoustic pressure on the Kirchhoff surface using a first-order backward difference. Then,

$$\left.\frac{\partial p'_e}{\partial \tau}\right|_{\tau^*} = \frac{p'^{n*}_e - p'^{n*-1}_e}{\Delta t} \tag{19}$$

where the superscript $n*$ is the time level such that, when multiplied by Δt, it gives a discrete time that is the closest to the emission time τ_e^*. This is only an approximation provided that Δt is sufficiently small. Hence we do not perform interpolations for the exact emission time data. No difficulties have been experienced with this. The gradient of the acoustic pressure is calculated using the same finite difference formulas as the flow solver. At this point the observer time is considered the same as the flow solver. Hence, for the discrete acoustic pressure at the observer point and time, we can write

$$p'[\boldsymbol{x}, n\Delta t] = \frac{1}{4\pi}\sum_{e=1}^{NE} P_e\{[n - \mathrm{int}(R_e/c_\infty)]\Delta t\}\,\Delta S_e \tag{20}$$

where the operator int( ) rounds the real argument to the closest integer. The time level $n - \mathrm{int}(R_e/c_\infty)$ in Eq. (20) is identical to the time level $n*$ that appears in Eq. (19).

It is possible to realize that each surface element e at time t of the Euler solver will contribute to the total acoustic pressure at the observer location a time period of R_e/c_∞ later. In other words, a signal of element e produced at time t will arrive at the observer at

$t + R_e/c_\infty$. Thus for the discretized acoustic pressure at the observer we can rewrite Eq. (20) as a recursive sum, where for $e = 1, 2, \ldots, NE$,

$$p'_{\text{new}}\{\mathbf{x}, [n + \text{int}(R_e/c_\infty)]\Delta t\} = (1/4\pi) P_e[n\Delta t]\Delta S_e + p'_{\text{old}}\{\mathbf{x}, [n + \text{int}(R_e/c_\infty)]\Delta t\} \quad (21)$$

Passing from Eq. (20) to Eq. (21), we have in effect modified the time level $n - \text{int}(R_e/c_\infty) = n*$ on the right-hand side of the former equation to be the time level n of the flow solver, so that the contributions of the Kirchhoff surface elements are integrated as soon as the Euler solution becomes available. This prevents long time histories of the acoustic pressure and its derivatives on the Kirchhoff surface from saving. Earlier, the Kirchhoff integrations are assumed to start at $n = n_{KS}$ and end at $n = n_{KE}$, and the initial values of pressure at the observer are set to zero, i.e., for $n \le n_{KS}$, and $e = 1, 2, \ldots, NE$,

$$p'\{\mathbf{x}, [n + \text{int}(R_e/c_\infty)]\Delta t\} = 0 \quad (22)$$

The time increment Δt is sometimes too small because of the numerical stability restrictions of the flow solver. Therefore, performing the Kirchhoff surface integrations at every time step may be unnecessary for a desired accuracy and consequently computationally expensive. Then to perform the integrations at every Kth time step, we rewrite Eq. (21) in the following form for $\text{mod}(n, K) = 0$ and $e = 1, 2, \ldots, NE$:

$$p'_{\text{new}}\{\mathbf{x}, [n + K\text{int}(R_e/Kc_\infty)]\Delta t\} = (1/4\pi) P_e[n\Delta t]\Delta S_e + p'_{\text{old}}\{\mathbf{x}, [n + K\text{int}(R_e/Kc_\infty)]\Delta t\} \quad (23)$$

By using this form of the integration we essentially lump the pressure contributions from surface elements in a time interval of K steps to be in a single bin. Furthermore, one can change the integer of the time argument of p' in this equation from $\{n + K\,\text{int}(R_e/Kc_\infty)\}$ to $\{s + \text{int}(R_e/Kc_\infty) - \text{int}(R_e/Kc_\infty)_{\min}\}$, where s is an integer counter that is advanced by 1 at every Kth step, starting from zero. During the postprocessing of the data, this argument is set back to $\{n_{KS} + s\,K + K\text{int}(R_e/Kc_\infty)\}$. This manipulation enables one to use the minimum possible memory for the observer pressure array in the code.

Equation (21) or (23) will give a transient field for some time periods after $n = n_{KS}$ and before $n = n_{KE}$. This is because we are essentially predicting future acoustic pressure contributions at the observer from each Kirchhoff surface element, which progressively sum up to the total acoustic pressure at the observer. The Kirchhoff results are then usable only in the range $n_{KS} + \Delta n_{\text{arr}} \le n \le n_{KE} - \Delta n_{\text{arr}}$, where $\Delta n_{\text{arr}} = \text{int}(R/c_\infty)_{\max} - \text{int}(R/c_\infty)_{\min}$.

An example result showing this is given in Fig. 2, where the Kirchhoff prediction and the exact solution at an upstream observer are shown together for a monopole placed in a $M_\infty = 0.2$ stream. For this example the acoustic pressure on a 192×128 element spherical Kirchhoff surface was obtained using the exact solution at discrete times (200 time levels per period), as if the solution had been given by the flow solver. The time derivative was obtained using Eq. (19), the pressure gradient was obtained using the same finite difference schemes as the flow solver, and the Kirchhoff integrations were performed at every fifth time level ($K = 5$ above). Because of the reason explained earlier, the Kirchhoff solution indicates a transient region after the start of the integrations.

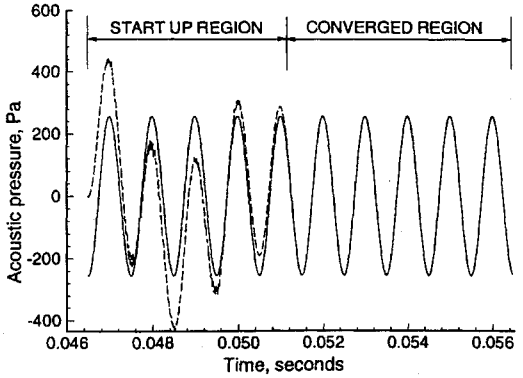

Fig. 2 Transient results of Kirchhoff integration. Moving monopole, $M = 0.2$, and $f = 1000$ Hz; ----, Kirchhoff solution and ——, exact solution.

The developed and coupled Kirchhoff code can accept multiple observer points and can perform integrations using multiple Kirchhoff surfaces for comparison purposes. Calculations for each Kirchhoff surface and observer point are carried out in a sequential manner. However, the integrand evaluations and summations over the discrete retarded times and surface elements are performed in parallel for each surface and observer.

III. Results and Discussion

In this section we present several test cases to validate the hybrid code. The first case is a radiation problem where a monopole-like source is placed in an open, finite length, circular duct with flow. Next, the method is tested against realistic noise sources in an engine inlet with and without mass flow, and results are compared with theory.

A. Radiation from an Open, Finite Length, Circular Duct

In this section, a rather simple yet significant problem is solved. A finite length, both-end-open, infinitely thin-walled, circular shell (duct) is placed in a uniform flow parallel to its axis. Therefore, the presence of the duct alone does not distort the flow. The duct is 1 m in both length and diameter ($L = D = 1$ m). A spatially distributed but very narrow, time-periodic mass source is placed at the geometrical center (origin) of the duct and generates spherical waves. This source is defined in cylindrical coordinates by

$$\dot{m} = 10 \exp[-80 \ln 2\,(x^2 + r^2)] \sin(2\pi f t) \quad (24)$$

For the computations, a frequency of $f = 750$ Hz, a uniform mesh with a cell spacing $\Delta x = \Delta r = 0.0125$ m, and a flow Mach number of 0.5 are used. These parameters imply a grid resolution of approximately 18 cells per wavelength in the upstream direction. The current scheme usually needs about 12 cells per wavelength to give results without significant dispersion and dissipation. Since the mass source is symmetric about the duct axis, the equations are solved in the axisymmetric mode, i.e., in a two-dimensional domain. The domain has flat outer boundaries that are only at about $2.7D$ distance in both $\pm x$ and r directions. The acoustic pressure is obtained by subtracting the mean pressure (p_∞) from the total pressure. The comparisons of only the Euler results are made here. We use the BEM solution of Myers[6] as the benchmark data. The BEM solution used 16 elements (rings) per wavelength and 15 s of Cray CPU time.

Because of the difficulty in matching the source strength of the finite difference algorithm to that of BEM, it was necessary to calibrate the results. Using the no-flow case with the same source parameters a single scaling factor was established by matching the peaks of the BEM solution and the current solution on the inner side of the duct wall. The scaling factor is $p_{\text{rms, BEM}}/p_{\text{rms, current}} = 7.75$.

Figure 3 illustrates the rms acoustic pressures along constant $r = 0.5 - 0.5\Delta r$ and $r = 0.5 + 0.5\Delta r$ m grid lines between which the duct wall is located at $r = 0.5$ m. The shielding effect of the duct wall is predicted very well when compared with the solution of BEM. This is clearly evident from Fig. 3. Note that the current solution is multiplied by the scaling factor 7.75. Therefore, the acoustic pressure predicted outside the duct wall has extremely low levels that were resolved by the current algorithm perfectly. There exist, however, some difference between the current result and that of BEM towards the edges of the duct wall. This is probably because in the current method the singular points are avoided using a cell-centered finite difference scheme. Consequently, it turns out that the edges of the duct are actually located at $x = -(0.5 \pm 0.5\Delta x)$ m, and $x = +(0.5 \pm 0.5\Delta x)$ m; i.e., there is an uncertainty of one cell size in the duct length. The difference between the results can also be attributed to the difference between the source definitions. The

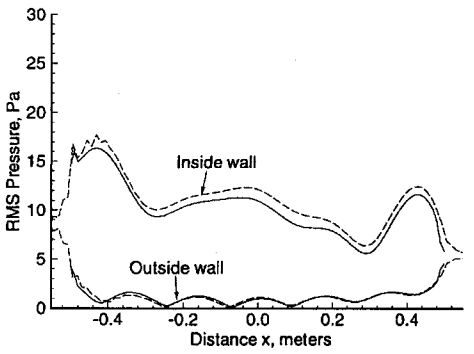

Fig. 3 RMS pressures along the inner and outer side of the duct wall, $M_\infty = 0.5$, and $f = 750$ Hz; - - - -, current solution and ——, boundary integral solution.[6]

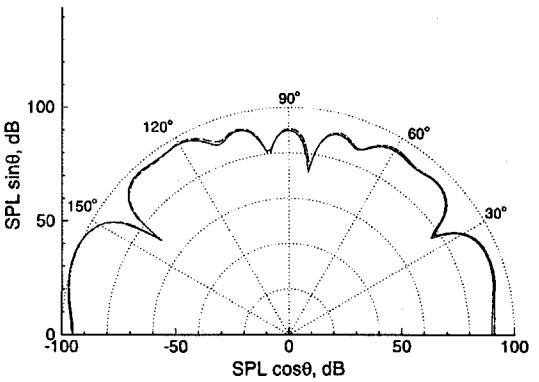

Fig. 4 Sound pressure level at $R = 2.5$ m in the x–r plane, $M_\infty = 0.5$, and $f = 750$ Hz; - - - -, current solution and ——, boundary integral solution.[6]

current solution was obtained using the source given by Eq. (24), whereas that of Myers used a monopole. The sound pressure level (SPL) comparison at a distance of $R = 2.5D$ in the x–r plane from the source location, however, indicates an excellent agreement at all angles, as shown in Fig. 4. This $R = 2.5D$ curve is in fact a circular arc that is very close to the outer boundaries. Therefore, this comparison is significant to show that the far-field boundary conditions work effectively.

B. Radiation from JT15D Engine Inlet Configuration

We present realistic ducted fan radiation results. The configuration chosen is the small JT15D turbofan engine inlet that has been extensively investigated both experimentally and numerically.[1,22,23] Rotor-bypass stator interactions of the blade passing frequency BPF in the JT15D are acoustically cut off over the engine operating range, and therefore rods were placed in front of the 28-blade fan to generate desired interaction tones at BPF for investigation purposes.[22,23] Modes generated using two different number of rods are considered here. The combination of the (0, 0) and (0, 1) modes with a 180-deg-phase difference is produced in the case of an array of 28 rods interacting with the fan, and the (13, 0) mode is generated in the case of an array of 41 rods.

The JT15D inlet has a duct radius of 0.2667 m at the fan stage, and there exists only a slight variation in the cross section through the inlet. In this paper, the cross section of the inlet duct is modified to be a constant for the no-flow cases. The purpose of this is to approximate the inner surface contour of the inlet to the flat surface of the flanged duct as much as possible, so that we can compare our results with the available flanged-duct radiation solutions used by Heidmann et al.[22] for their JT15D investigations. For the flow cases, the real JT15D inlet geometry[23] is used with only very minor modifications made to the inlet contour in the discontinuous slope regions inside the inlet and also on the outer wall away from the inlet lip to prevent strong acceleration of the flow. Also, in all of the cases presented later the centerbody is neglected. This is a common practice taken for the hard-walled ducts since there are no sound absorption mechanisms by the wall.[1,5] Therefore, for the no-flow cases presented here, the choice of the reference plane for the source specification is rather arbitrary. However, the current code is capable of solving problems with a centerbody. Example calculations for this are given in Özyörük and Long.[14]

1. Radiation of the (0, 0) and (0, 1) Modes: No Inlet Flow

The first comparison with the flanged-duct radiation solution[22] involves the far-field directivity yielded by the superimposed (0, 0) and (0, 1) modes each having a 3-kPa amplitude and a BPF of 3150 Hz (6750 rpm) with no inlet flow. Although the source amplitude is chosen arbitrarily high, we do not expect any nonlinearities because of the mass flow absence. The cutoff ratios of the modes are $\xi_{0,0} = \infty$ and $\xi_{0,1} = 4.05$.

Since there is no flow in the inlet, at the source plane it is more appropriate to specify the momentum rather than the acoustic pressure directly. The momentum at the source plane is $\rho V = \rho_\infty V'$. The acoustic particle velocity V' is easily obtained by inserting the pressure expressed by Eq. (7) into the linearized momentum equations and analytically integrating the resultant equations. The other dependent variables are solved from the interior equations. The pressure is then found from the equation of state. Since the problem is symmetric about the inlet axis, the equations are integrated in the axisymmetric mode.

Figure 5 shows the geometry, the mesh system around it, and the two Kirchhoff surfaces used for far-field predictions. It should be noted that the representative cowl has a thin inlet lip. The Kirchhoff surfaces terminate at the cowl wall near the leading edge. Thus the hybrid method actually uses an open Kirchhoff surface. This is equivalent to assuming that any contributions to the far field from the remainder of the surface are negligible, if it were a closed surface. Notice that the grid system is fine in the very near field and is coarse exterior to the Kirchhoff surfaces. This is because we are interested in resolving the waves accurately only in the near field and passing the solution to the Kirchhoff routine of the current hybrid method. The mesh spacing in the fine region is such that there exist approximately 15 cells per wavelength along the inlet axis. The Kirchhoff surfaces are constructed just by rotating the grid lines 360 deg at the Kirchhoff surfaces locations, forming 128 elements in the circumferential direction. The number of elements on each surface in the transverse direction is 44. The Kirchhoff integrations are performed at every 12th [i.e., $K = 12$ in Eq. (23)] time step of the flow solver, for which the time increment is taken $\Delta t = 0.5/(384\text{BPF})$ s. Therefore, one period is represented by 64 discrete points in the Kirchhoff results. The nondimensional frequency parameter $kr = 15.5$ at the fan stage.

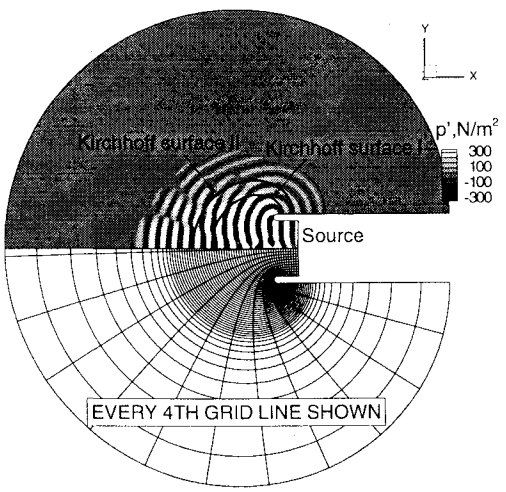

Fig. 5 Grid system, the Kirchhoff surfaces, and the acoustic pressure field of the (0, 0) + (0, 1) modes. The JT15D geometry modified, BPF = 3150 Hz, $M_\infty = M_f = 0$, and $(kr)_f = 15.5$.

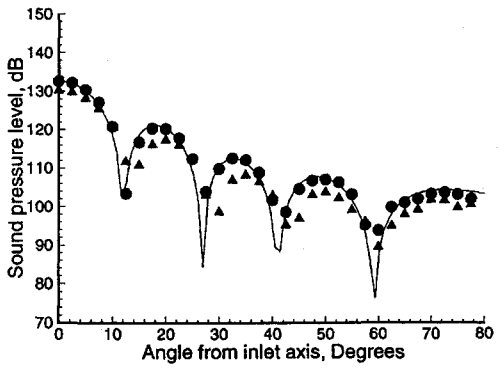

Fig. 6 Far-field sound pressure level of the (0, 0) + (0, 1) modes; BPF = 3150 Hz, $M_\infty = M_f = 0$, and $(kr)_f = 15.5$: •, prediction, Kirchhoff surface I; △, Kirchhoff surface II; and ——, flanged duct solution.[22]

Figure 5 also shows an instantaneous view of the acoustic pressure contours generated by the (0, 0) + (0, 1) modes. The resulting far-field directivities at a distance of 30.5 m in the x–r plane, as predicted by the two Kirchhoff surfaces, are shown in Fig. 6 together with the analytical flanged-duct solution given by Eq. (3) of Heidmann et al.[22] The rms of the current solution yielded by the inner Kirchhoff surface and that of the analytical solution were scaled to match at the inlet axis (zero angle). This resulted in excellent agreement at the other angles, despite the open Kirchhoff surface and the approximate geometry (see Fig. 5) as compared with flanged duct. However, the outer Kirchhoff predictions are about 2–4 dB lower as compared with the inner Kirchhoff results. We suspect that the relatively poor predictions by the outer Kirchhoff surface are mainly caused by the increased surface element areas across which we assume the acoustic pressure is constant. However, if the grid lines emanating from inside the inlet diverged from each other at the same rate as the angles between the directions of the radiated pressure lobes, the outer surface should have been expected to give as accurate results as the inner surface. In other words, how the pressure varies in the transverse direction plays a role in the difference between the results of the two Kirchhoff surfaces.

2. Radiation of the (13, 0) Mode: No Inlet Flow

In this section we compare the current predictions for the spinning (13, 0) mode with theory (flanged-duct solution[22]). There is no flow in the inlet and BPF is the same as the previous case. The cutoff ratio is $\xi_{13,0} = 1.04$, and the radiated main lobe is expected to be away from the inlet axis.

The grid used for the (0, 0) and (0, 1) modes was rotated to construct the three-dimensional grid for the (13, 0) mode calculations such that 16 cells existed for each circumferential lobe. Since an acoustic field driven by a single m mode is periodic at every 360 deg/m, the three-dimensional full Euler equations and the nonreflecting far-field boundary conditions were solved only in one of the 13 periodic domains ($m = 13$) in the circumferential direction. However, the Kirchhoff integrations were performed for the entire 360 deg as required. The same two Kirchhoff surface locations as in the previous section were used.

Figure 7 illustrates an instantaneous view of the acoustic pressure contours on the inner Kirchhoff surface. The pattern of the spinning pressure waves is evident. Figure 8 compares the predicted far-field SPLs with the flanged-duct solution. The latter was scaled to match the prediction given by the inner Kirchhoff surface at 55 deg from the inlet axis. The maximum of the flanged-duct solution for this mode occurs at about 90 deg from the inlet axis. It is known from experimental and numerical results[1,22] that the far-field SPL levels off and goes down well before 90 deg from the inlet axis. Of course the geometry used (see Fig. 5) for the numerical simulations is only a representative model to the flanged-duct. Thus the current method is believed to have predicted the real case reasonably well. However, the variation of the predicted SPL is not as smooth below 35 deg, where the very low acoustic pressure levels were probably contaminated by numerical errors.

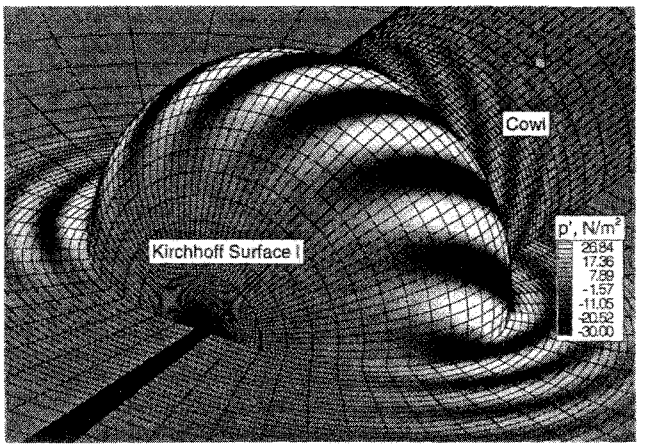

Fig. 7 Pressure contours of the (13, 0) mode on the inner Kirchhoff surface; BPF = 3150 Hz, $M_\infty = M_f = 0$, and $(kr)_f = 15.5$.

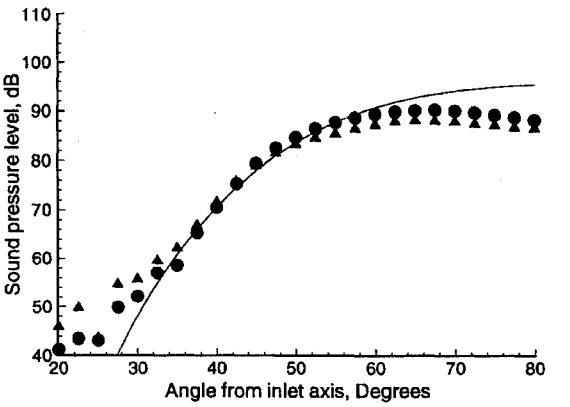

Fig. 8 Far-field sound pressure level of the (13, 0) mode; BPF = 3150 Hz, $M_\infty = M_f = 0$, and $(kr)_f = 15.5$: •, prediction, Kirchhoff surface I; △, Kirchhoff surface II; and ——, flanged duct solution.[22]

3. Radiation of the Combined (0, 0) and (0, 1) Modes with Flow

Finally in this section, we present results for the real JT15D inlet geometry at the conditions $M_\infty = 0.204$ and 15 kg/s mass flow through the inlet. These parameters are kept constant and the combination of the (0, 0) and (0, 1) modes with a 180-deg-phase difference is considered for two different cases of BPFs to study the convergence of the Kirchhoff results given by two different surfaces. This study is considerably valuable to see the effects of using an open Kirchhoff surface, as well as the effects of the mesh resolution on the Kirchhoff surfaces.

The computational mesh is shown in Fig. 9 along with the Kirchhoff surfaces. Notice that the far-field boundaries are extremely close to the inlet entrance and the mesh is significantly fine. Before the time-accurate calculations, steady-state computations are required by the approach of the current hybrid method. It is always very difficult to attain rapid steady-state solutions on such fine meshes. A multigrid convergence acceleration procedure that retains the fourth-order spatial accuracy of the hybrid method has been developed to circumvent slow convergence associated with low-Mach-number flows, fine meshes, and high-resolution schemes. Steady-state calculations use the one-dimensional characteristic based boundary conditions of Giles[24] at the fan face to achieve very accurate mass flow rates (MFR) as well as to aid convergence. This procedure and the multigrid method are described in Özyörük.[15]

The residual was driven 13 orders of magnitude down from its initial value via the multigrid method to obtain the steady-state solution shown in Fig. 10. Also shown in this figure is an instantaneous view of the acoustic pressure contours produced by the application of the (0, 0) + (0, 1) modes with BPF = 4 kHz and $A_{nm\mu} = 0.3$ kPa each. The time increment for the acoustic calculations was taken

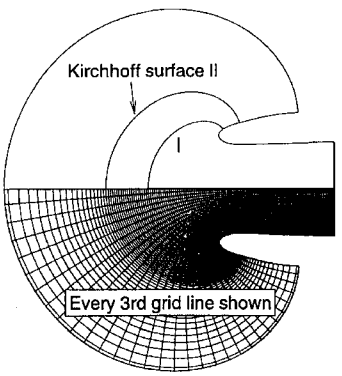

Fig. 9 384 × 96 cell grid system around the JT15D inlet and the Kirchhoff surfaces.

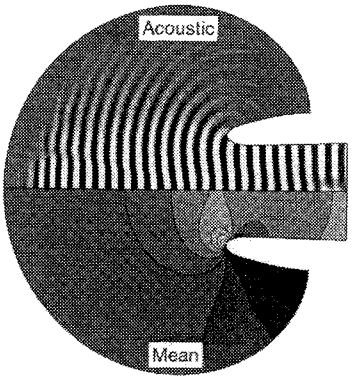

Fig. 10 Steady pressure and the acoustic field driven by the (0, 0) + (0, 1) modes; BPF = 4 kHz, MFR = 15 kg/s, M_∞ = 0.204, M_f = 0.159, and $(kr)_f$ = 19.7.

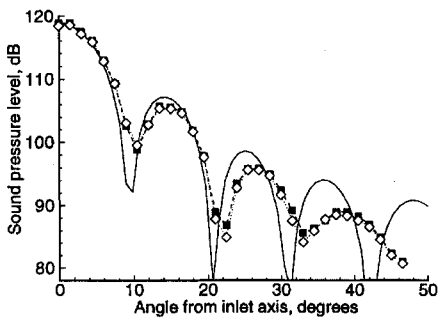

Fig. 11 Far-field sound pressure level of the combined (0, 0) and (0, 1) modes; BPF = 4 kHz, MFR = 15 kg/s, M_∞ = 0.204, M_f = 0.159, and $(kr)_f$ = 19.7 ■, Kirchhoff surface I; ◇, Kirchhoff surface II; and ——, flanged duct solution.[22]

$\Delta t = 0.5/(384\,\text{BPF})$. It is evident that in the coarse mesh region (near the outer boundaries) the waves are attenuated because the mesh resolution is not sufficient to support the wave frequency, as well as the spherical spreading effects.

Figures 11 and 12 show the far-field SPLs for 4 kHz [$(kr)_f$ = 19.7] and 5 kHz [$(kr)_f$ = 24.6], respectively, as predicted by the two Kirchhoff surfaces. Also shown in these figures are the analytical flanged-duct solutions of Heidmann et al.[22] The predictions of the inner and outer Kirchhoff surfaces are in very good agreement for the 4-kHz case, for which the number of cells per wavelength along the inlet axis is approximately 14. However, the 5-kHz case presents some slight discrepancies. For this case the number of cells per wavelength is about 12 along the axis. Notice by comparing the two figures that the higher the frequency, the higher the number of the radiated (0, 0) + (0, 1) lobes. About five lobes occur at 4 kHz in 50 deg, whereas six lobes occur at 5 kHz. Therefore, as the frequency is increased, the transverse resolution on the Kirchhoff surface appears

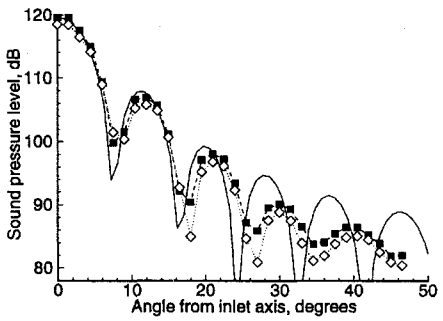

Fig. 12 Far-field sound pressure level of the combined (0, 0) and (0, 1) modes; BPF = 5 kHz, MFR = 15 kg/s, M_∞ = 0.204, M_f = 0.159, and $(kr)_f$ = 24.6: ■, Kirchhoff surface I; ◇, Kirchhoff surface II; and ——, flanged duct solution.[22]

to worsen more quickly than the axial resolution of the CFD mesh. Therefore, the occurrence of the discrepancies is more susceptible to the transverse resolution on the Kirchhoff surface. One important conclusion from this study is that the nonuniform flowfields between the two Kirchhoff surfaces have minimal effects on the far-field sound.

In both cases the flanged-duct solutions represent the directivities fairly well as compared with the numerical simulations. The differences are mainly caused by the theory's same-flow-everywhere correction and the assumption of a constant cross-sectional duct.

C. Requirement for Computational Resources

The three-dimensional calculations [spinning (13, 0) mode on a 384 × 48 × 16 grid with 2 Kirchhoff surfaces and 32 observer points] presented in this paper required about 5.3 h of CPU time on the 256-node CM-5 (Connection Machine 5 of the Thinking Machines Corporation) in the time-shared mode and 600 MBytes of memory. The calculations were performed over 20,000 time steps. The code essentially spent approximately 3.2 μs per grid point per time step for calculating the acoustic pressures at 32 observer points using 2 Kirchhoff surfaces. Kirchhoff integrations alone spent approximately 25% of this time. It should be noted that the current method can accept multiple circumferential and radial mode because of its three dimensionality and time-domain approach. Therefore, it is believed that complex problems of ducted fan noise radiation can be analyzed in reasonable computer times, considering the high-level governing equations.

IV. Conclusions

A temporally and spatially fourth-order accurate, three-dimensional Euler solver has been developed and coupled to a moving surface Kirchhoff method for noise predictions from ducted fans. The code has been tested against radiation problems from realistic geometries and compared with flanged-duct radiation solutions. The method has the advantage of modeling the geometry and nonuniform background flow effects on the radiation process with no limitations of the number of modes that can be specified as the source, unlike the frequency-domain methods. The current method is also capable of modeling nonlinear effects.

The code has been written in CM-Fortran, which is very similar to high-performance Fortran language, which makes the code portable to other parallel computing platforms, such as SP-2, with only minor modifications. The current code needs about 3.2 μs per grid point per time step on a time-shared 256-node CM-5 computer for noise predictions at multiple observers using multiple Kirchhoff surfaces.

The method is currently being tested against experimental data. Also, the incorporation of a time-domain impedance condition on the inlet wall is under way.

Acknowledgments

The authors would like to acknowledge support from NASA Langley Research Center Grant NAG-1-1367. Computer resources were provided by the Numerical Aerodynamics Simulation Program at

the NASA Ames Research Center and the National Center for Supercomputing Applications at the University of Illinois at Urbana–Champaign. We would especially like to thank F. Farassat and M. K. Myers for their suggestions and discussions on some of the issues in this paper.

References

[1]Eversman, W., Parret, A. V., Preisser, J. S., and Silcox, R. J., "Contributions to the Finite Element Solution of the Fan Noise Radiation Problem," *Transactions of the American Society of Mechanical Engineers*, Vol. 107, April 1985, pp. 216–223.

[2]Parret, A. V., and Eversman, W., "Wave Envelope and Finite Element Approximations for Turbofan Noise Radiation in Flight," *AIAA Journal*, Vol. 24, No. 5, 1986, pp. 753–760.

[3]Philbrick, D. A., and Topol, D. A., "Development of a Fan Noise Design System, Part 1: System Design and Source Modeling," AIAA Paper 93-4415, Oct. 1993.

[4]Topol, D. A., "Development of Fan Noise Design System, Part 2: Far-Field Radiation and System Evaluation," AIAA Paper 93-4415, Oct. 1993.

[5]Hsu, C.-H., Spence, P. L., and Farassat, F., "Ducted Fan Noise Prediction Based on a Hybrid Aerodynamic-Aeroacoustic Technique," CEAS/AIAA Paper 95-075, June 1995.

[6]Myers, M. K., "Boundary Integral Formulations for Ducted Fan Radiation Calculations," CEAS/AIAA Paper 95-076, June 1995.

[7]Dougherty, R. P., "Nacelle Acoustic Design by Ray Tracing in Three Dimensions," AIAA Paper 96-1773, May 1996.

[8]Martinez, R., "Aeroacoustic Diffraction and Dissipation by a Short Propeller Cowl in Subsonic Flight," NASA CR-190801, April 1993.

[9]Farassat, F., and Myers, M. K., "Extension of Kirchhoff's Formula for Radiation from Moving Surfaces," *Journal of Sound and Vibration*, Vol. 123, June 1988, pp. 451–460.

[10]Özyörük, Y., and Long, L. N., "A Hybrid Scheme for Noise Radiation from Ducted Fans," *Proceedings of NOISE-CON'93*, edited by H. H. Hubbard, Noise Control Foundation, New York, 1993, pp. 577–582.

[11]Özyörük, Y., and Long, L. N., "A Navier–Stokes/Kirchhoff Method for Noise Radiation from Ducted Fans," AIAA Paper 94-0462, Jan. 1994.

[12]Bayliss, A., and Turkel, E., "Far Field Boundary Conditions for Compressible Flow," *Journal of Computational Physics*, Vol. 48, Nov. 1982, pp. 182–199.

[13]Tam, C. K. W., and Webb, J. C., "Dispersion-Relation-Preserving Finite Difference Schemes for Computational Acoustics," *Journal of Computational Physics*, Vol. 107, Aug. 1993, pp. 262–281.

[14]Özyörük, Y., and Long, L. N., "A New Efficient Algorithm for Computational Aeroacoustics on Parallel Processors," *Journal of Computational Physics*, Vol. 125, No. 1, 1996, pp. 135–149.

[15]Özyörük, Y., "Sound Radiation from Ducted Fans Using Computational Aeroacoustics On Parallel Computers," Ph.D. Thesis, Dept. of Aerospace Engineering, Pennsylvania State Univ., University Park, PA, 1995.

[16]Tyler, J. M., and Sofrin, T. G., "Axial Flow Compressor Noise Studies," *SAE Transactions*, Vol. 70, 1962, pp. 309–332.

[17]Eversman, W., "Radiated Noise of Ducted Fans," DGLR/AIAA Paper 92-02-139, May 1992.

[18]Xue, Y., and Lyrintzis, A. S., "Rotating Kirchhoff Method for Three-Dimensional Transonic Blade-Vortex Interaction Hover Noise," *AIAA Journal*, Vol. 32, No. 7, 1994, pp 1350–1359.

[19]Jaeger, S. M., and Korkan, K. D., "On the Prediction of Far-Field Computational Aeroacoustics of ADP Advanced Propellers," AIAA Paper 90-3996, Oct. 1990.

[20]Lyrintzis, A. S., "Review: The Use of the Kirchhoff's Method in Computational Aeroacoustics," *Journal of Fluids Engineering*, Vol. 116, Dec. 1994, pp. 665–675.

[21]Myers, M. K., and Hausmann, J. S., "On the Application of the Kirchhoff Formula for Moving Surfaces," *Journal of Sound and Vibration*, Vol. 139, May 1990, pp. 174–178.

[22]Heidmann, M. F., Saule, A. V., and McArdle, J. G., "Analysis of Radiation Patterns of Interaction Tones Generated by Inlet Rods in the JT15D Engine," AIAA Paper 79-0581, March 1979.

[23]Preisser, J. S., Silcox, R. J., Eversman, W., and Parret, A. V., "Flight Study of Tone Radiation Patterns Generated by Inlet Rods in a Small Turbofan Engine," AIAA Paper 84-0499, Jan. 1984.

[24]Giles, M. B., "Nonreflecting Boundary Conditions for Euler Equation Calculations," *AIAA Journal*, Vol. 28, No. 12, 1990, pp. 2050–2058.